Robotica (2012) volume 30, pp. 433–447. © Cambridge University Press 2011
doi:10.1017/S0263574711000683

Stiffness optimization of a novel reconfigurable parallel kinematic manipulator

Zhongzhe Chi† and Dan Zhang†‡*

†*University of Ontario Institute of Technology, 2000 Simcoe Street North, Oshawa, ON L1H 7K4, Canada*
‡*Harbin Institute of Technology Shenzhen Graduate School, Shenzhen University Town, Xili, Shenzhen, China*

(Received in Final Form: June 10, 2011; accepted June 9, 2011. First published online: July 20, 2011)

SUMMARY

This paper proposes a novel design of a reconfigurable parallel kinematic manipulator used for a machine tool. After investigating the displacement and inverse kinematics of the proposed manipulator, it is found that the parasitic motions along x-, y-, and θ_z-axes can be eliminated. The system stiffness of the parallel manipulator is conducted. In order to locate the highest system stiffness, single and multiobjective optimizations are performed in terms of rotation angles in x- and y-axes and translation displacement in z-axis. Finally, a case study of tool path planning is presented to demonstrate the application of stiffness mapping. Through this integrated design synthesis process, the system stiffness optimization is conducted with Genetic Algorithms. By optimizing the design variables including end-effector size, base platform size, the distance between base platform and middle moving platform, and the length of the active links, the system stiffness of the proposed parallel kinematic manipulator has been greatly improved.

KEYWORDS: Design; Parallel manipulators; Stiffness optimization; Stiffness control; Kinematic modeling.

1. Introduction

A serial robot is an open-loop mechanical arm consisting of a number of links connected with prismatic or revolute joints, which is very commonly used in industry. One of the most significant advantages of serial robots is the large workspace. However, they still have some unavoidable drawbacks, such as the low stiffness due to the open-loop mechanism, errors accumulated by joints, and the heavy actuators' weight they have to carry while working. In the contrary, a parallel manipulator has closed-loop kinematic chains to connect an end-effector platform and a base by at least two kinematic chains.[1] The parallel kinematic manipulators have significant advantages over traditional serial robots.[2,3] First of all, the actuators can be mounted on the base, which can significantly reduce the moving mass, resulting in higher load capacity. Furthermore, parallel manipulators have higher stiffness, since the end-effector is supported by several legs. Parallel manipulators also have higher accuracy, since there is no error accumulation.[4] However, the main disadvantage of the parallel manipulators is the limited workspace.

* Corresponding author. E-mail: dan.zhang@uoit.ca

Research and development in parallel robotic machines generally focus on 6 degrees of freedom (6-DOF) and recently focus more on 3-DOF manipulators. The former study is based on the Steward platform.[5,6] Since most machining tasks require a maximum of five axes, 3-DOF parallel robotic machine design with three axes is becoming popular. Combination of a 3-DOF structure with a gantry system forms a five-axis machine with both large workspace and dexterity. Therefore, more and more 3-DOF parallel manipulators have been proposed in recent years. There are structures with 3-PUU (for prismatic, universal, and universal joints),[7] 3-UPU (for universal, prismatic, and universal joints),[8] 3-PRS (for prismatic, revolute, and spherical joints),[9–12] and 3-CRR (for cylindrical, revolute, and revolute joints),[13] etc. Among which the 3-PRS becomes one of the popular designs since it provides two rotational and one translational motions. Li and Xu[9–12] have done an intensive research on 3-PRS parallel manipulator. However, research on a 3-PRS reconfigurable parallel manipulator is quite few.

Reconfigurable manufacturing system is designed at the outset for rapid change in structure, as well as in hardware and software components, in order to quickly adjust production capacity and functionality.[14] In general, the reconfigurability of Parallel Kinematic Machines (PKM) system can be realized at modular level, which is the idea using one or more off the shelf modules to configure different structures or even a manufacturing cell[15,16] and its configuration design includes the selections of modules and the determination of geometric dimensions in some specific modules.[17,18] In contrast to the modular reconfigurable system, the continuous reconfigurable system has an adjustable mechanical system, which can provide continuous various configurations to the parallel kinematic manipulator. Apart from its low cost, high flexibility, good dynamics, and large workspace, it is also desirable that the continuous reconfigurable PKMs will not have many modular parts and do not need to be reinstalled. In this paper, the reconfigurable manipulator is implemented by a middle moving platform driven by motors, thus to provide continuous configurations.

Stiffness is one of most important performance specification of parallel kinematic machines (PKM) particularly for the use of machine tools.[19–21] Therefore, it is quite necessary to perform the stiffness modeling and to evaluate the PKM in the early design stage.[22] In this paper, the stiffness models are established based on inverse kinematics, and stiffness optimization is discussed.

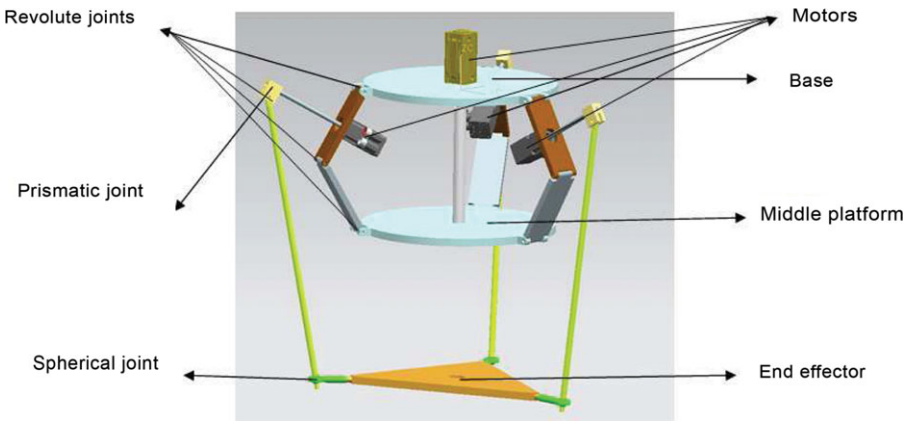

Fig. 1. (Colour online) 3-DOF reconfigurable parallel kinematic manipulator.

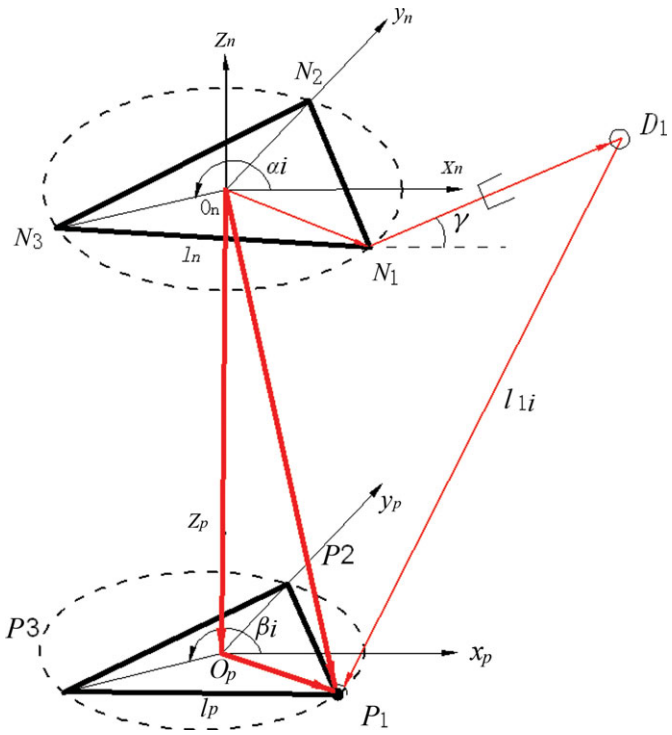

Fig. 2. (Colour online) Simplified schematic diagram of a 3-DOF reconfigurable PKM.

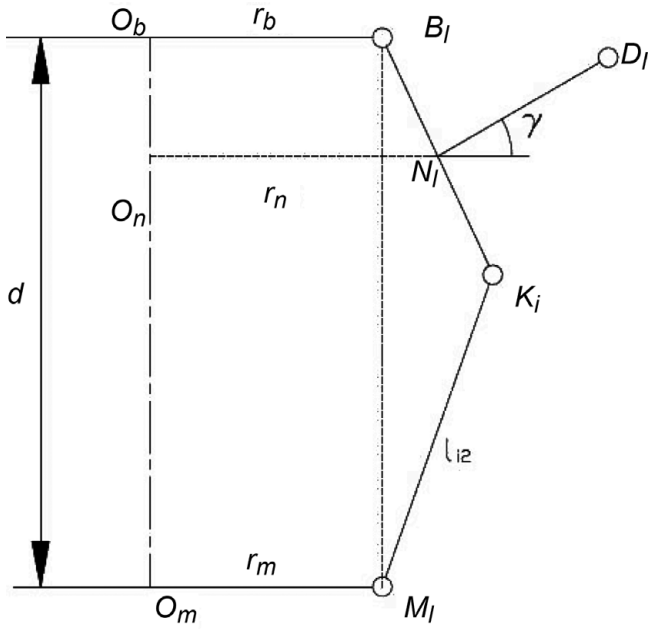

Fig. 3. Simplified schematic diagram of the reconfigurable drive section.

2. Design Description of a Reconfigurable Parallel Kinematic Machine

The Compter-Aided Design (CAD) model of a 3-PRS PKM is shown in Fig. 1. This manipulator consists of a fixed base and two mobile platforms. Among the two mobile platforms, the bottom one is a end-effector. The motions of the end-effector are generated by three motors with leadscrews mounted between the base platform and middle mobile platform connected by three legs having PRS. This is a traditional PRS manipulator design. The spindle located in end-effector can hold various tools for drilling, milling, or deburring.

In traditional design, the middle platform is always fixed, but in this novel design, the middle mobile platform is actuated by a motor mounted on the top of the base platform, which can create different configurations of the PKM. When this manipulator is do drilling, milling, or deburring, generally the top motor is not working, only the three side motors give the motions the manipulator, which can enable specify inverse kinematics, workspace, and stiffness mapping. But if various workspace and stiffness mapping are required, the top motor can adjust the displacement between base platform and middle mobile platform, which give various angles of the three motors. Compared with traditional modular reconfigurable PKM, this novel design can provide continuous reconfiguration of this PKM and get rid of reinstallation.

3. Kinematic Analysis

3.1. Displacement representation

As shown in Fig. 2, this system can be simplified into a simple 3-RPS (for revolute, prismatic, and spherical joints) parallel manipulator, which has two platforms including the adjustable middle platform expressed by $N_1N_2N_3$ and the end-effector labeled by $P_1P_2P_3$. The coordinate system of the inertial frame is denoted as $O_n - X_nY_nZ_n$, in which

https://doi.org/10.1017/S0263574711000683 Published online by Cambridge University Press

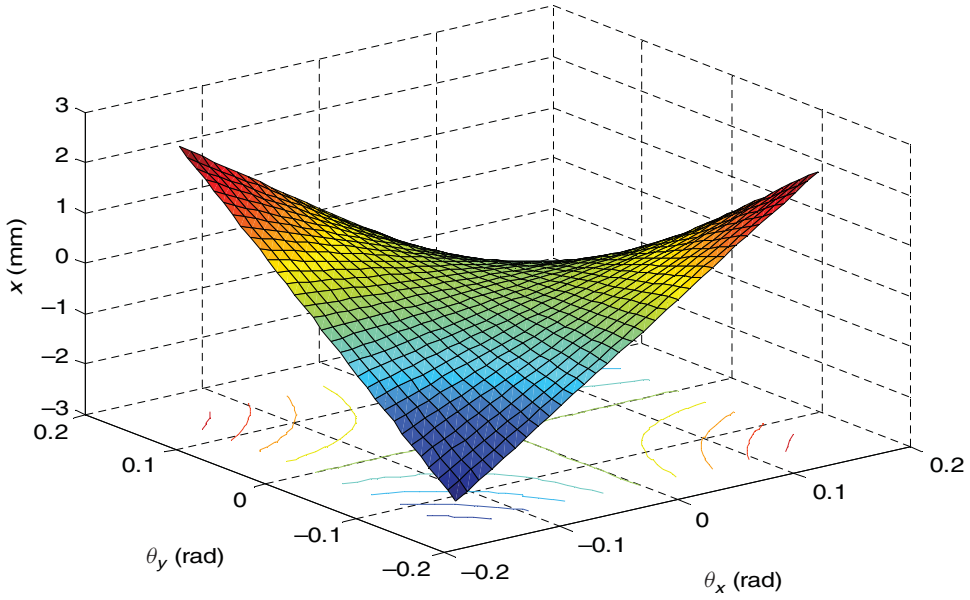

Fig. 4. (Colour online) Parasitic motion along X-axis.

Y_n-axis is aligned with the O_nN_2, and while those of the moving frame is labeled by $O_p - X_pY_pZ_p$ where Y_p-axis is coincident with the point P_2.

The following parameters define other details of the structure:

- α_i and β_i define the O_iN_i and O_iP_i directions, which are measured from x_n and x_p.
- l_n and l_p are denoted by the sizes of the base and end-effector platform.
- α is the direction of actuators to the base platform.
- l_{1i} is the length of the active link.

The simplified schematic diagram of the reconfigurable drive section is represented in Fig. 3. The displacement between base platform $B_1B_2B_3$ and middle platform $N_1N_2N_3$ is denoted by d, which is actuated by a prismatic actuator, and the radius of the middle platform is r_n. The relationship between reconfigurable displacement d and system parameters angle γ and link length l_{i_2} can be revealed by Eq. (1) from Fig. 3

$$\gamma = \arccos \frac{d}{2l_{i2}}. \tag{1}$$

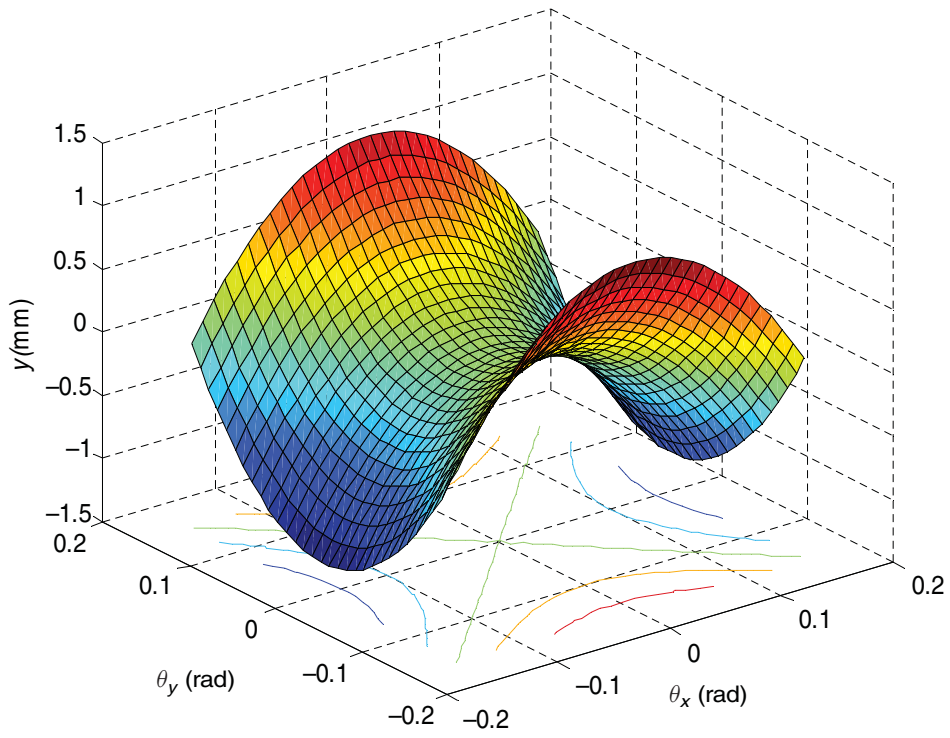

Fig. 5. (Colour online) Parasitic motion along Y-axis.

https://doi.org/10.1017/S0263574711000683 Published online by Cambridge University Press

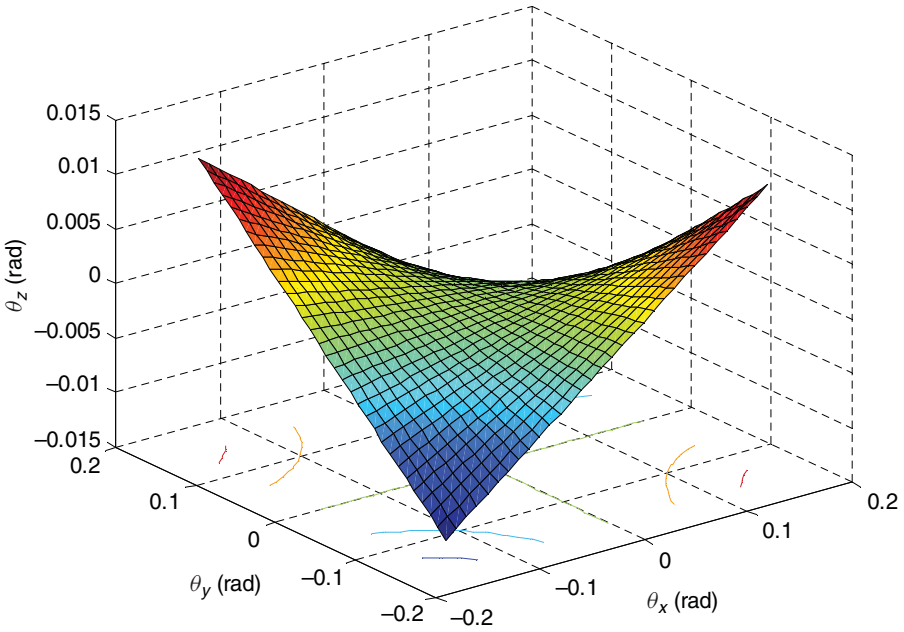

Fig. 6. (Colour online) Parasitic motion along θ_z.

The motion of end-effector of O_p can be denoted by $(\theta_x, \theta_y, \theta_z, x_p, y_p, z_p)$, where $\theta_x, \theta_y, \theta_z$ are the rotations and x_p, y_p, z_p are the translations. The rotation representation is defined as (1) rotation by an angle θ_z about z-axis followed by (2) rotation by an angle θ_y about y-axis, and (3) rotation by an angle θ_z about z-axis. This yields the rotation matrix:

$$\begin{aligned} R_p &= R_p(x,\theta)R_p(y,\theta)R_p(z,\theta), \\ &= \begin{bmatrix} 1 & 0 & 0 \\ 0 & c\theta_x & -s\theta_x \\ 0 & s\theta_x & c\theta_x \end{bmatrix} \begin{bmatrix} c\theta_y & 0 & s\theta_y \\ 0 & 1 & 0 \\ -s\theta_y & 0 & c\theta_y \end{bmatrix} \begin{bmatrix} c\theta_z & -s\theta_z & 0 \\ s\theta_z & c\theta_z & 0 \\ 0 & 0 & 1 \end{bmatrix}, \\ &= \begin{bmatrix} c\theta_y c\theta_z & -c\theta_y s\theta_z & s\theta_y \\ s\theta_x s\theta_y + c\theta_x s\theta_z & -s\theta_x s\theta_y s\theta_z + c\theta_x c\theta_z & -s\theta_x c\theta_y \\ -c\theta_x s\theta_y c\theta_z + s\theta_x c\theta_z & c\theta_x s\theta_y s\theta_z + s\theta_x c\theta_z & c\theta_x c\theta_y \end{bmatrix}, \end{aligned} \tag{2}$$

where c, s denote the cosine and sine functions, respectively. Therefore, the pose of the end-effector with respect to the coordinate system $o_p - x_p y_p z_p$ can be expressed as

$$\begin{aligned} T_p^n &= \begin{bmatrix} \mathrm{R}_p & \mathrm{P}_p \\ 0 & 1 \end{bmatrix} \\ &= \begin{bmatrix} c\theta_y c\theta_z & -c\theta_y s\theta_z & s\theta_y & x_p \\ s\theta_x s\theta_y + c\theta_x s\theta_z & -s\theta_x s\theta_y s\theta_z + c\theta_x c\theta_z & -s\theta_x c\theta_y & y_p \\ -c\theta_x s\theta_y c\theta_z + s\theta_x c\theta_z & c\theta_x s\theta_y s\theta_z + s\theta_x c\theta_z & c\theta_x c\theta_y & z_p \\ 0 & 0 & 0 & 1 \end{bmatrix}. \end{aligned} \tag{3}$$

The location of the connection of the end-effector and link l_{1i}

$$\mathrm{p}_{p_i}^n = \mathrm{R}_p \mathrm{p}_{p_i}^p + \mathrm{p}_p^n, \tag{4}$$

where $\mathrm{p}_{p_i}^n$ is the vector from O_n, the base platform to P_i. $\mathrm{p}_{p_i}^p$ is the P_i point vector from O_p, the moving platform

$$\begin{cases} \mathrm{p}_{p_i}^n = \begin{bmatrix} x_{p_i}^n & y_{p_i}^n & z_{p_i}^n \end{bmatrix}^{\mathrm{T}}, \\ \mathrm{p}_{p_i}^p = [l_p c\beta_i \quad l_p s\beta_i \quad 0\,]^{\mathrm{T}}, \\ p_p^n = [x_p \quad y_p \quad z_p\,]^{\mathrm{T}}, \\ R_p = \begin{bmatrix} c\theta_y c\theta_z & -c\theta_y s\theta_z & s\theta_y \\ s\theta_x s\theta_y + c\theta_x s\theta_z & -s\theta_x s\theta_y s\theta_z + c\theta_x c\theta_z & -s\theta_x c\theta_y \\ -c\theta_x s\theta_y c\theta_z + s\theta_x c\theta_z & c\theta_x s\theta_y s\theta_z + s\theta_x c\theta_z & c\theta_x c\theta_y \end{bmatrix}. \end{cases} \tag{5}$$

Substituting Eq. (5) to Eq. (4) yields

$$\begin{aligned} P_{pi}^n = &\begin{bmatrix} c\theta_y c\theta_z & -c\theta_y s\theta_z & s\theta_y \\ s\theta_x s\theta_y + c\theta_x s\theta_z & -s\theta_x s\theta_y s\theta_z + c\theta_x c\theta_z & -s\theta_x c\theta_y \\ -c\theta_x s\theta_y c\theta_z + s\theta_x c\theta_z & c\theta_x s\theta_y s\theta_z + s\theta_x c\theta_z & c\theta_x c\theta_y \end{bmatrix} \\ &\times \begin{bmatrix} l_p c\beta_i \\ l_p s\beta_i \\ 0 \end{bmatrix} + \begin{bmatrix} x_p \\ y_p \\ z_p \end{bmatrix}. \end{aligned} \tag{6}$$

Therefore,

$$\begin{aligned} &\begin{bmatrix} x_{pi}^n \\ y_{pi}^n \\ z_{pi}^n \end{bmatrix} \\ &= \begin{bmatrix} l_p c\theta_y c\theta_z c\beta_i - l_p c\theta_y s\theta_z s\beta_i + x_p \\ l_p(s\theta_x s\theta_y c\theta_z + c\theta_x s\theta_z)c\beta_i + l_p(-s\theta_x s\theta_y s\theta_z + c\theta_x s\theta_z)s\beta_i + y_p \\ l_p(-c\theta_x s\theta_y c\theta_z + s\theta_x c\theta_z)c\beta_i + l_p(c\theta_x s\theta_y s\theta_z + s\theta_x c\theta_z)s\beta_i + z_p \end{bmatrix}. \end{aligned} \tag{7}$$

3.2. *Constraint of the revolution joints*

The mechanism analyzed above has translation and rotation motions with respect to the reference frame, and it requires

https://doi.org/10.1017/S0263574711000683 Published online by Cambridge University Press

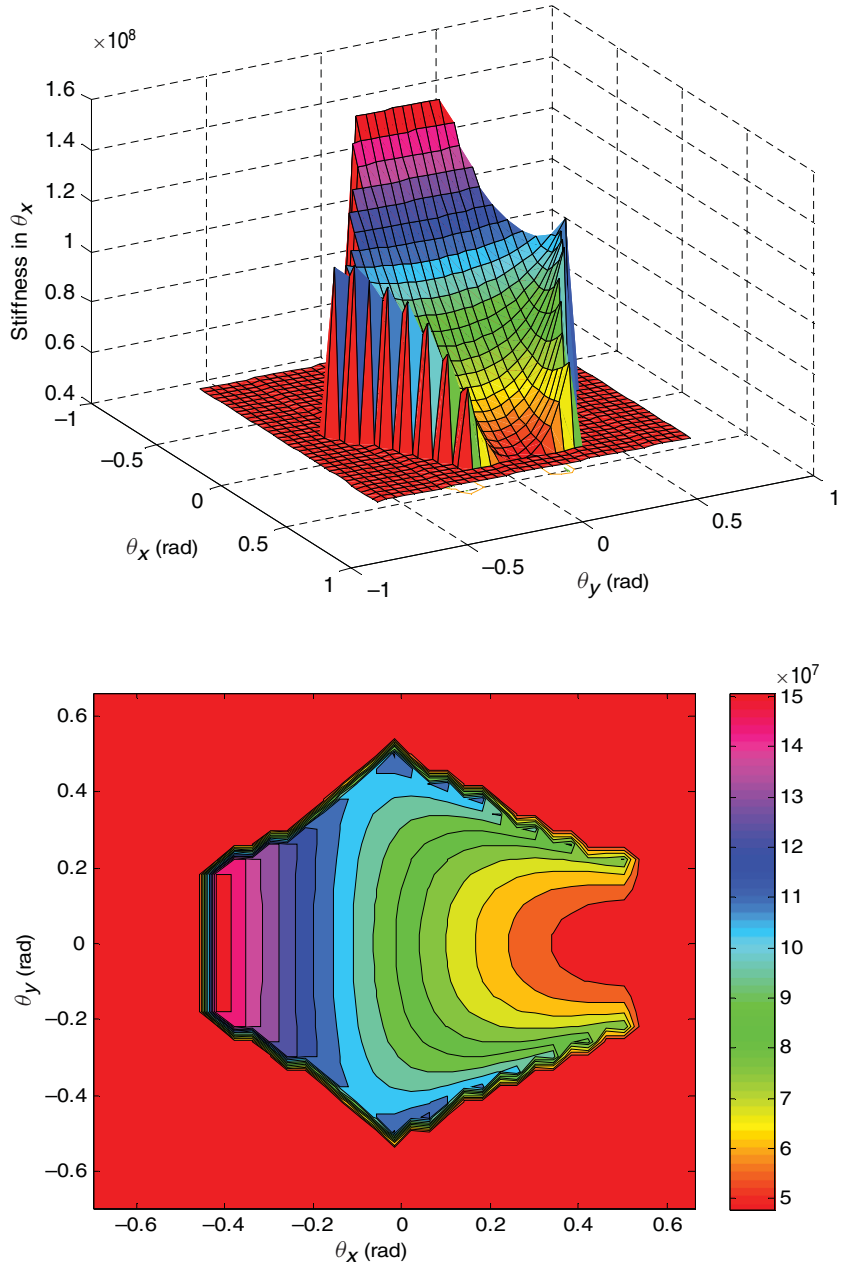

Fig. 7. (Colour online) θ_x stiffness distribution along θ_x and θ_y (when $z = 500$ mm).

six variables, namely, $x_p, y_p, z_p, \theta_x, \theta_y,$ and θ_z. However, this PKM is a 3-DOF device as described above that means there are only three independent parameters chosen as θ_x, θ_y, z_p and the others θ_z, z_x, z_y are selected as dependant parameters. These dependant parameters can be found by the constrain of the revolution joints D_i, which means the points O_p, P_i, D_i and N_i are in the same plane, which gives

$$x_{pi}^n = \frac{y_{ei}^n}{\tan\beta_i}. \tag{8}$$

From Eq. (7), where

$$\begin{cases} x_{pi}^n = l_p c\theta_y c\theta_z c\beta_i - l_p c\theta_y s\theta_z s\beta_i + x_p, \\ y_{pi}^n = l_p(s\theta_x s\theta_y c\theta_z + c\theta_x s\theta_z)c\beta_i \\ \qquad + l_p(-s\theta_x s\theta_y s\theta_z + c\theta_x c\theta_z)s\beta_i + y_p. \end{cases} \tag{9}$$

Thus,

$$\begin{cases} \dfrac{\sqrt{3}l_p c\theta_y c\theta_z - l_p c\theta_y s\theta_z + 2x_p}{-3l_p(s\theta_x s\theta_y c\theta_z + c\theta_x s\theta_z) - \sqrt{3}l_p(-s\theta_x s\theta_y s\theta_z + c\theta_x c\theta_z) + 2\sqrt{3}y_p l_p c\theta_y s\theta_z + x_p = 0,} = 1, \\ \dfrac{-\sqrt{3}l_p c\theta_y c\theta_z + l_p c\theta_y s\theta_z + 2x_p}{-3l_p(s\theta_x s\theta_y c\theta_z + c\theta_x s\theta_z) - \sqrt{3}l_p(-s\theta_x s\theta_y s\theta_z + c\theta_x c\theta_z)s\beta_i + 2\sqrt{3}y_p} = 1. \end{cases} \tag{10}$$

https://doi.org/10.1017/S0263574711000683 Published online by Cambridge University Press

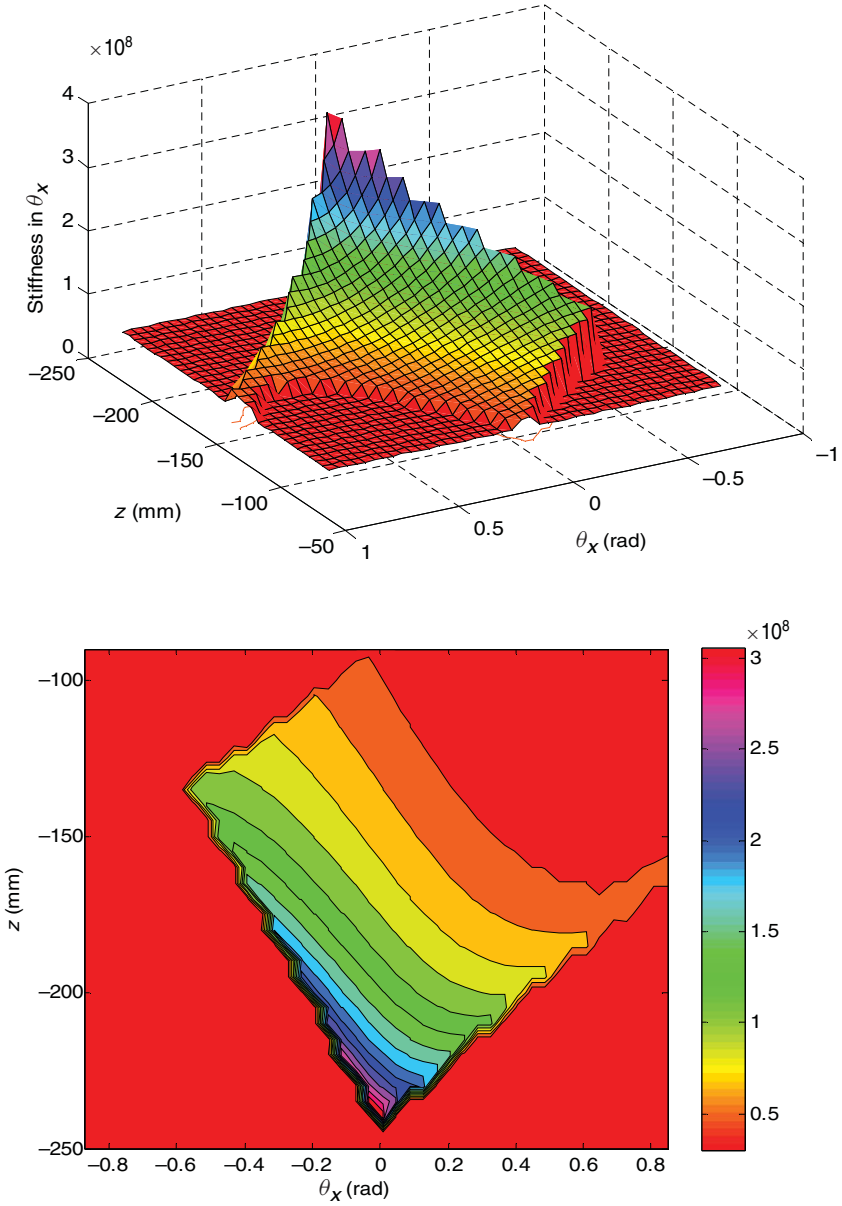

Fig. 8. (Colour online) θ_x stiffness distribution along θ_x and z (when $\theta_y = 0$).

Solving Eq. (10) by x_p, y_p, θ_z gives the constraint equations

$$\begin{cases} \theta_z = \arctan\left(\dfrac{-s\theta_x s\theta_y}{c\theta_x + c\theta_y}\right), \\ x_p = -\dfrac{\sqrt{3}}{3} l_p c\theta_y c\theta_z, \\ y_p = \dfrac{\sqrt{3}}{6}(c\theta_x c\theta_z - c\theta_y\theta_z - s\theta_x s\theta_y s\theta_z). \end{cases} \tag{11}$$

The motions along the x, y, and θ_z can be deemed as parasitic motions, which occur only specified with θ_x, θ_y and independent with z-axis from Eq. (11). As illustrated in Fig. 4, when there are rotations about x- and y-axes at range of -0.2–0.2 radians, the parasitic motion along x is only from –2 to 2 mm. The similar conclusion of parasitic motion along y can be revealed from Fig. 5, which shows that when the rotations about x- and y-axes are -0.2 to 0.2, the motion along y is from -1 1 mm. Figure 6 shows that at the same range of rotation motion about x and y, the translation along z is from -0.01 to 0.01 m. Therefore, the parasitic motions of x, y, and θ_z can be neglected.

3.3. *Inverse kinematics*

The inverse kinematics is the problem to determine the displacement of the actuated variables for a known position and orientation of the end-effector. The joint motions can be derived from another loop

$$\left|\overrightarrow{O_n P_i}\right| = \left|\overrightarrow{\mathrm{O_n N_i}} + \overrightarrow{\mathrm{N_i D_i}} + \overrightarrow{\mathrm{D_i} P_i}\right| \ (i = 1, 2, 3), \tag{12}$$

$$\begin{cases} x_{pi}^n = l_n c\alpha_i + v_i c\gamma c\alpha_i + l_{x1i}, \\ y_{pi}^n = l_n s\alpha_i + v_i c\gamma s\alpha_i + l_{y1i}, \\ z_{pi}^n = v_i s\gamma + l_{z1i}. \end{cases} \tag{13}$$

https://doi.org/10.1017/S0263574711000683 Published online by Cambridge University Press

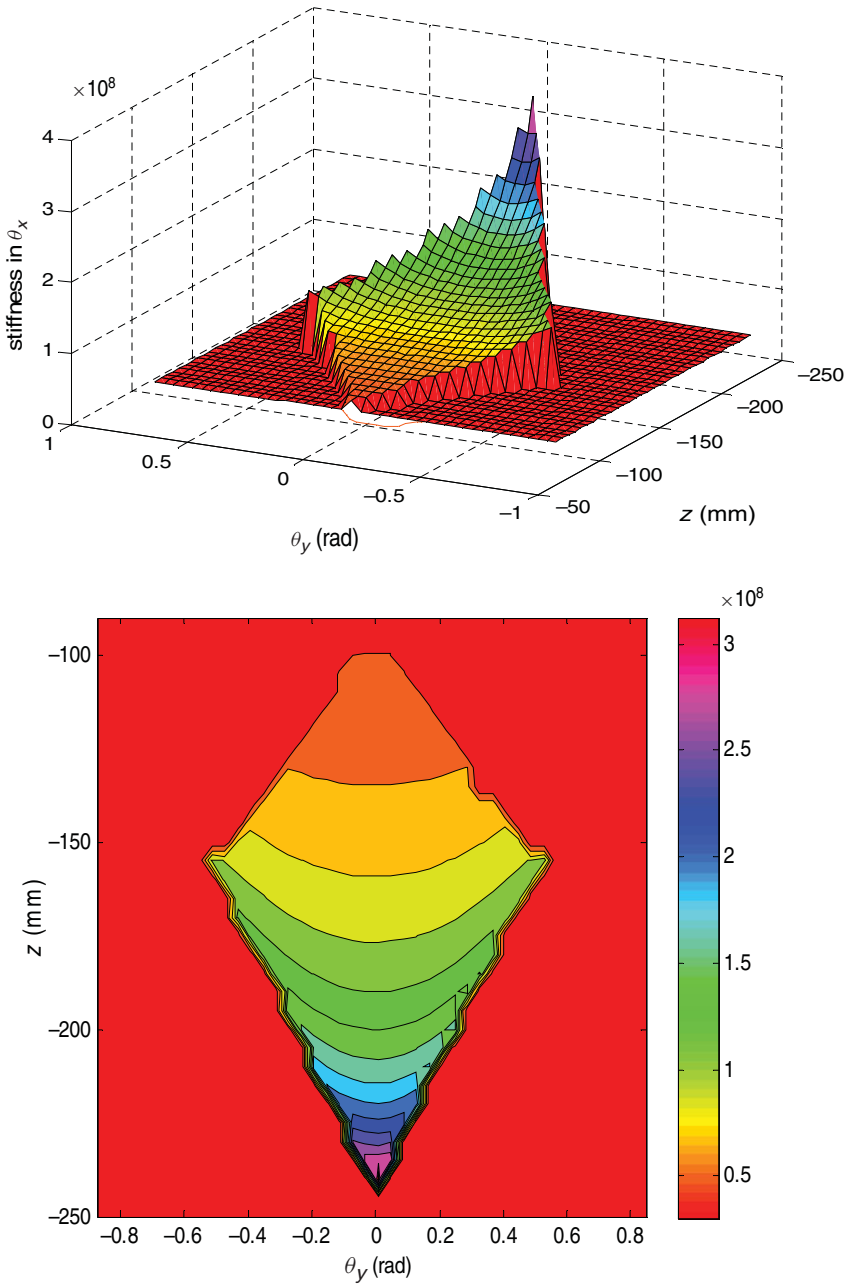

Fig. 9. (Colour online) θ_x stiffness distribution along θ_y and z (when $\theta_x = 0$).

Substituting Eq. (7) to Eq. (13) allows

$$\begin{cases} l_{x1i} = l_p c\theta_y c\beta_i - l_n c\alpha_i - v_i c\gamma c\alpha_i, \\ l_{y1i} = l_p c\beta_i s\theta_x s\theta_y + l_p s\beta_i c\theta_x - l_n s\alpha_i + v_i c\gamma s\alpha_i, \\ l_{z1i} = -l_p c\beta_i c\theta_x s\theta_y + l_p s\beta_i s\theta_x + z_p - v_i s\gamma. \end{cases} \quad (14)$$

From the constrain of the fixed length of the links $D_i E_i$, the following equation can be derived:

$$l_{x1i}^2 + l_{y1i}^2 + l_{z1i}^2 = l_{1i}^2. \quad (15)$$

From Eq. (13)

$$\begin{cases} l_{x1i} = x_{Ai} + x_{Bi} v_i, \\ l_{y1i} = y_{Ai} + y_{Bi} v_i, \\ z l_{z1i} = z_{Ai} + z_{Bi} v_i, \end{cases} \quad (16)$$

where

$$\begin{cases} x_{Ai} = x_{pi}^n - l_n c\alpha_i, \\ x_{B1} = -c\gamma c\alpha_i, \\ y_{A1} = y_{pi}^n - l_n s\alpha_i, \\ y_{B1} = -c\gamma s\alpha_i, \\ z_{A1} = z_{pi}^n, \\ z_{B1} = -s\gamma. \end{cases} \quad (17)$$

Substituting Eqs. (16) and (17) to Eq. (15) yields

$$v_{a1} v_1^2 + v_{b1} v_1 + v_{c1} = 0, \quad (18)$$

https://doi.org/10.1017/S0263574711000683 Published online by Cambridge University Press

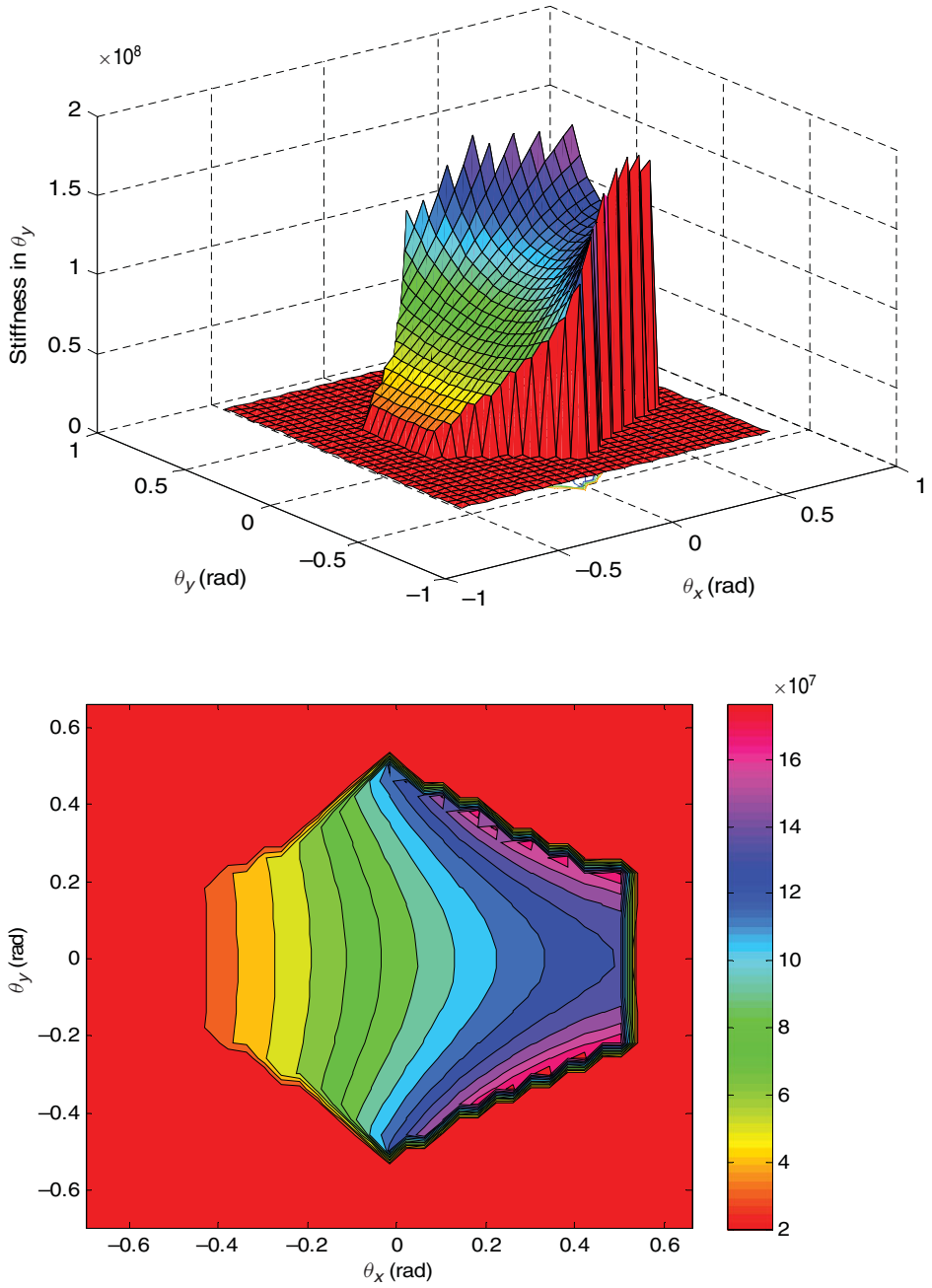

Fig. 10. (Colour online) θ_y stiffness distribution along θ_x and θ_y (when $z = 500$ mm).

where

$$\begin{cases} v_{ai} = x_{Bi}^2 + y_{Bi}^2 + z_{Bi}^2, \\ v_{Bi} = 2(x_{Ai}x_{Bi} + y_{Ai}y_{Bi} + z_{Ai}z_{Bi}), \\ v_{ci} = x_{Ai}^2 + y_{Ai}^2 + z_{Ai}^2 - l_{1i}^2. \end{cases} \tag{19}$$

The inverse kinematics can be derived by

$$v_i = \frac{-v_{b1} \pm \sqrt{v_{b1}^2 - 4v_{a1}v_{c1}}}{2v_{a1}}. \tag{20}$$

3.4. Jacobian equation

Jacobian matrix can be defined as the matrix of all first-order partial derivatives of a vector valued function as shown in Eq. (21), in which the motions of this PKM are represented by the independent parameters

$$\begin{bmatrix} \delta x_{p_i}^n \\ \delta y_{p_i}^n \\ \delta z_{p_i}^n \end{bmatrix} = [J_i] \begin{bmatrix} \partial\theta_x \\ \partial\theta_y \\ \partial z_p \end{bmatrix}. \tag{21}$$

The Jacobian matrix for vector P_{pi}^n can be obtained by differentiating Eq. (7) yields

$$J_i = \begin{bmatrix} 0 & -l_p s\theta_y c\beta_i & 0 \\ l_p c\beta_i c\theta_x s\theta_y - l_p s\beta_i s\theta_x & l_p c\beta_i s\theta_x c\theta_y & 0 \\ l_p c\beta_i s\theta_x s\theta_y + l_p s\beta_i c\theta_x & -l_p c\beta_i c\theta_x c\theta_y & 1 \end{bmatrix}. \tag{22}$$

https://doi.org/10.1017/S0263574711000683 Published online by Cambridge University Press

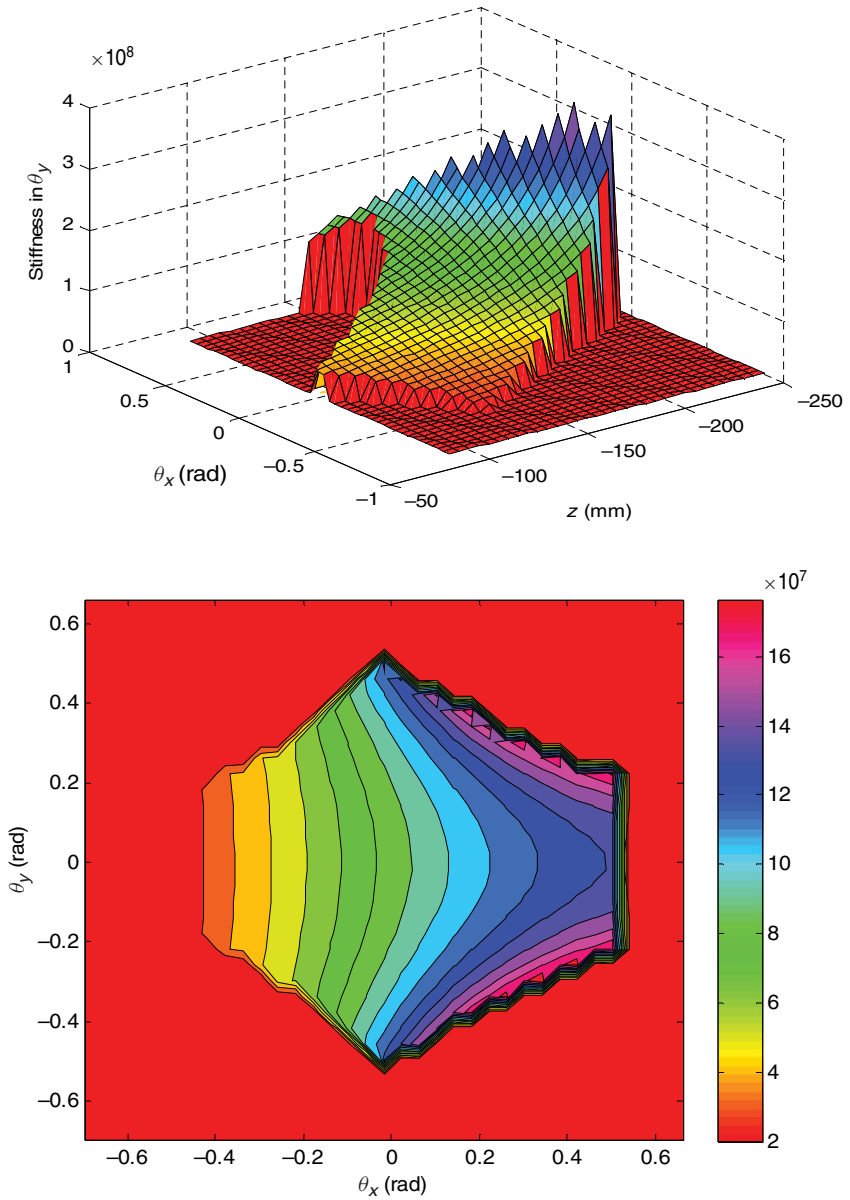

Fig. 11. (Colour online) θ_y stiffness distribution along θ_x and z (when $\theta_y = 0$).

Differentiating Eq. (15) yields

$$2l_{x1i}\frac{\delta l_{x1i}}{\delta x_{pi}^n} + 2l_{y1i}\frac{\delta l_{y1i}}{\delta x_{pi}^n} + 2l_{z1i}\frac{\delta l_{z1i}}{\delta x_{pi}^n} = 0. \tag{23}$$

Substituting Eq. (13) to Eq. (23) gives

$$\begin{cases} \dfrac{\delta v_i}{\delta x_{pi}^n} = \dfrac{l_{x1i}}{c\gamma c\alpha_i l_{xli} + c\gamma s\alpha_i l_{yli} + s\gamma l_{z1i}}, \\ \dfrac{\delta v_i}{\delta y_{pi}^n} = \dfrac{l_{y1i}}{c\gamma c\alpha_i l_{xli} + c\gamma s\alpha_i l_{yli} + s\gamma l_{z1i}}, \\ \dfrac{\delta v_i}{\delta z_{pi}^n} = \dfrac{l_{z1i}}{c\gamma c\alpha_i l_{xli} + c\gamma s\alpha_i l_{yli} + s\gamma l_{z1i}}. \end{cases} \tag{24}$$

Thus,

$$[\delta v_i] = \begin{bmatrix} \dfrac{l_{x1i}}{\Delta_i} & \dfrac{l_{y1i}}{\Delta_i} & \dfrac{l_{z1i}}{\Delta_i} \end{bmatrix} \cdot \begin{bmatrix} \delta x_{p_i}^b \\ \delta y_{p_i}^b \\ \delta z_{p_i}^b \end{bmatrix} (i = 1, 2, 3), \tag{25}$$

where

$$\Delta_i = l_{xi1}c\gamma c\alpha_i + l_{yi2}c\gamma s\alpha_i - l_{zi2}s\gamma. \tag{26}$$

Therefore, the Jacobian matrix for the actuator can be represented by

$$[J_{v_i}] = \begin{bmatrix} \dfrac{l_{xi1}}{\Delta_i} & \dfrac{l_{yi2}}{\Delta_i} & \dfrac{l_{zi3}}{\Delta_i} \end{bmatrix}. \tag{27}$$

Substituting Eq. (21) to Eq. (25)

$$\begin{bmatrix} \partial v_1 \\ \partial v_2 \\ \partial v_3 \end{bmatrix} = \begin{bmatrix} J_{v_1} \\ J_{v_2} \\ J_{v_3} \end{bmatrix} \begin{bmatrix} \delta x_{p_i}^b \\ \delta y_{p_i}^b \\ \delta z_{p_i}^b \end{bmatrix} = \begin{bmatrix} J_{v_1} \\ J_{v_2} \\ J_{v_3} \end{bmatrix} [J_i] \begin{bmatrix} \partial \theta_x \\ \partial \theta_y \\ \partial z_p \end{bmatrix}. \tag{28}$$

https://doi.org/10.1017/S0263574711000683 Published online by Cambridge University Press

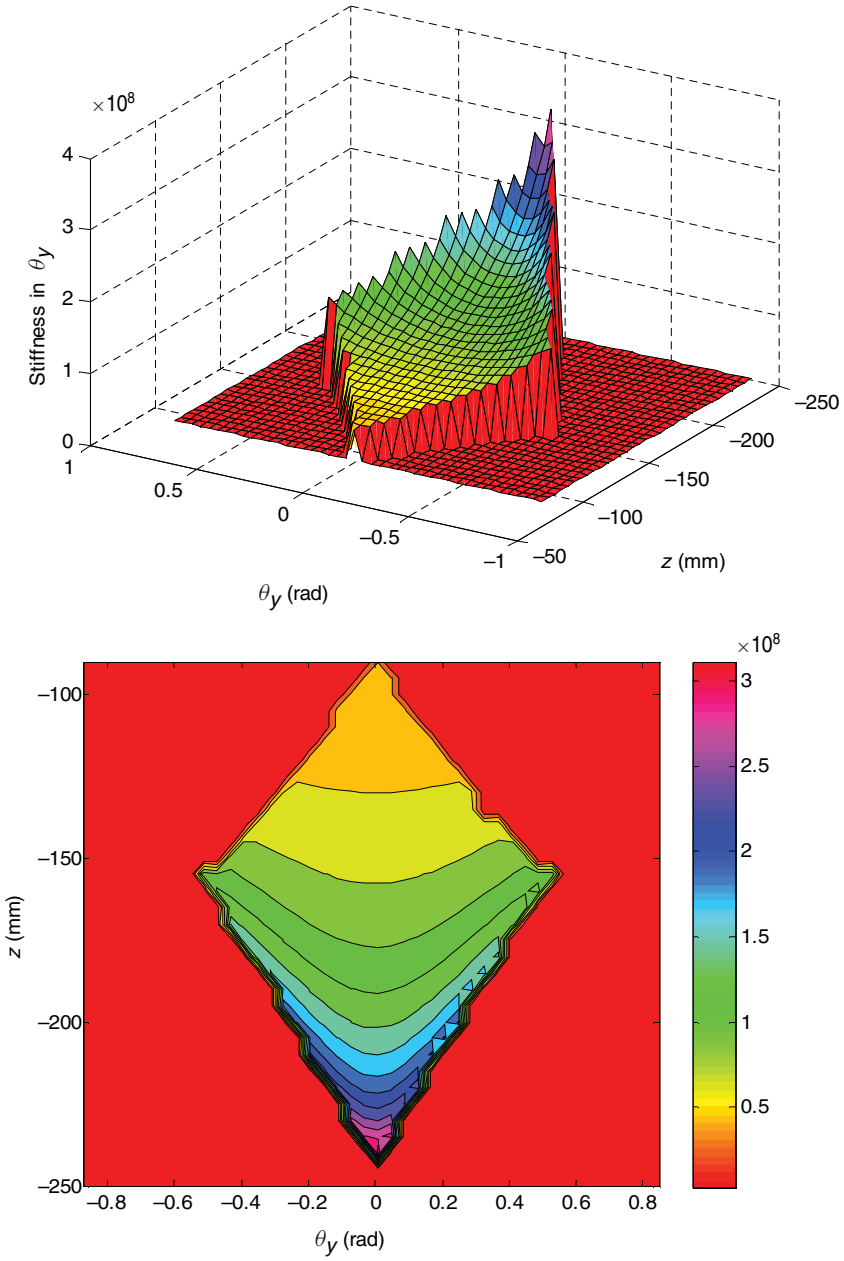

Fig. 12. (Colour online) θ_y stiffness distribution along θ_y and z (when $\theta_x = 0$).

Finally, we get

$$J = \begin{bmatrix} J_{v_1} \\ J_{v_2} \\ J_{v_3} \end{bmatrix} [J_i]. \tag{29}$$

Here, J is called the Jacobian of actuations.

4. Stiffness Analysis

4.1. Stiffness modeling

The stiffness of a parallel mechanism is dependent on the actuator's stiffness, the leg's structure and material, the platform and base's stiffness, the geometry of the structure, the topology of the structure, and the end-effector position and orientation. To simplify this problem, the joints and links of this system are assumed to be a rigid.

The stiffness of a PKM is related to a wrench acting on the moving platform including the forces and moments to its deformation

$$\boldsymbol{w} = \boldsymbol{K}\delta x, \tag{30}$$

where $\boldsymbol{w}$ is the wrench vector showing the torques and forces acting on the moving platform, which can be represented as $\boldsymbol{w} = [\tau_x \quad \tau_y \quad \tau_z \quad F_x \quad F_y \quad F_z]^{\mathrm{T}}$, while $\boldsymbol{\delta} x$ is the vector representing the angular and linear deformation of the platform, shown as $\delta \boldsymbol{x} = [\dot{\theta}_x \quad \dot{\theta}_y \quad \dot{\theta}_z \quad \dot{x} \quad \dot{y} \quad \dot{z}]^{\mathrm{T}}$ and $\boldsymbol{K}$ is the generalized stiffness matrix.

The wrench acting on the moving platform is related to the forces and moments at the actuators by the transpose of the Jacobian matrix J

$$\boldsymbol{w} = \boldsymbol{J}^{\mathrm{T}}\boldsymbol{f}, \tag{31}$$

$$\delta \boldsymbol{q} = \boldsymbol{J}\delta x, \tag{32}$$

https://doi.org/10.1017/S0263574711000683 Published online by Cambridge University Press

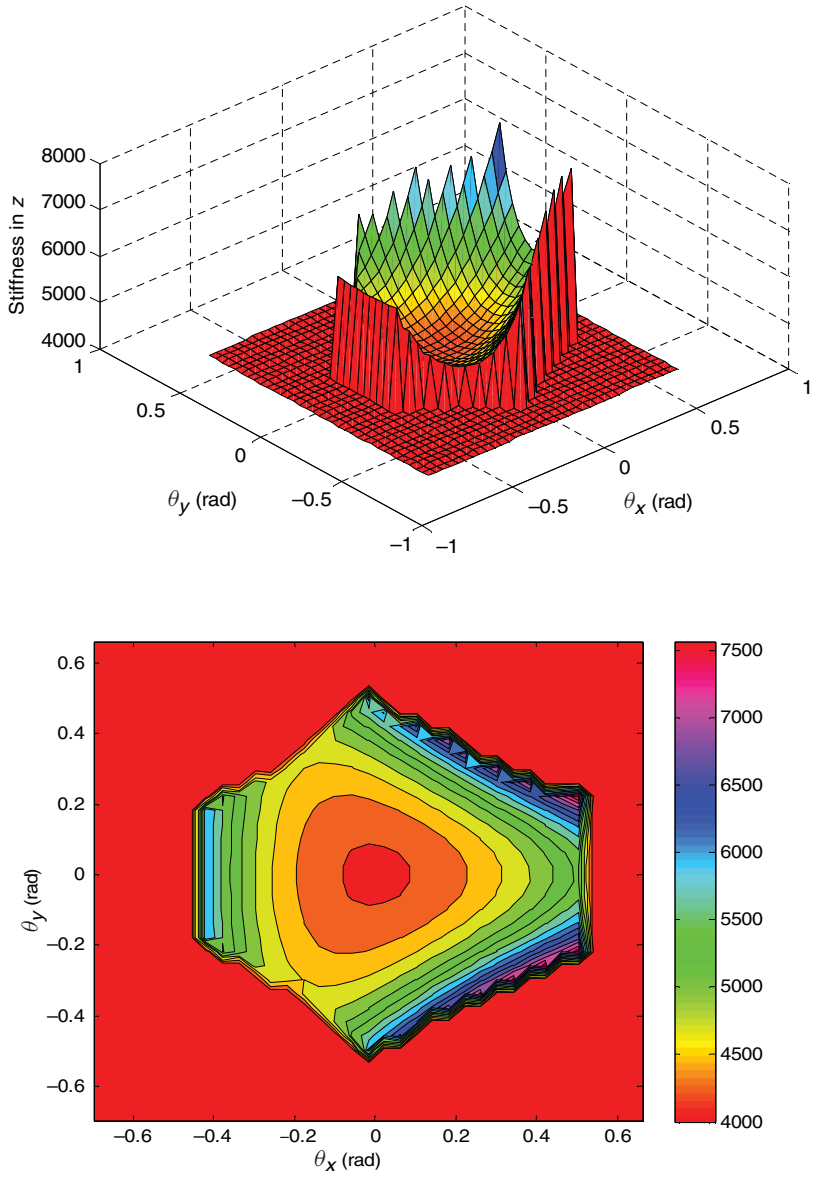

Fig. 13. (Colour online) z stiffness distribution along θ_x and θ_y (when $z = 500$ mm).

where $\boldsymbol{f}$ is the vector showing the actuators forces and moments, while $\delta\boldsymbol{q}$ is the deformation of the actuators. The actuator forces and displacements can be expressed by Hooke's law as shown in Eq. (33)

$$\boldsymbol{f} = \boldsymbol{K}_J \delta q, \tag{33}$$

where $K_J = \text{diag}[k_1 \quad k_2 \quad k_3]$ is the actuator's stiffness matrix of the parallel manipulator, while k_1, k_2, and k_3 represent the joint stiffness of each actuator. Substituting Eqs. (32) and (33) to Eq. (31) yield

$$\boldsymbol{w} = \boldsymbol{K}\delta\boldsymbol{x}, \tag{34}$$

where the generated stiffness matrix $\boldsymbol{K}$ can be given as

$$\boldsymbol{K} = \boldsymbol{J}^{\mathrm{T}}\boldsymbol{K}_J\boldsymbol{J}. \tag{35}$$

4.2. Stiffness evaluation of the tripod parallel kinematic machines

The architecture parameters of this tripod PKM are shown in Table I.

From Eq. (34), the stiffness can be expressed by

$$\begin{bmatrix} \tau_x \\ \tau_y \\ \tau_z \\ F_x \\ F_y \\ F_z \end{bmatrix} = \begin{bmatrix} k_{11} & k_{12} & k_{13} & k_{14} & k_{15} & k_{16} \\ k_{21} & k_{22} & k_{23} & k_{24} & k_{25} & k_{26} \\ k_{31} & k_{32} & k_{33} & k_{34} & k_{35} & k_{36} \\ k_{41} & k_{42} & k_{43} & k_{44} & k_{45} & k_{46} \\ k_{51} & k_{52} & k_{53} & k_{54} & k_{55} & k_{56} \\ k_{61} & k_{62} & k_{63} & k_{64} & k_{65} & k_{66} \end{bmatrix} \begin{bmatrix} \dot{\theta}_x \\ \dot{\theta}_y \\ \dot{\theta}_z \\ \dot{x} \\ \dot{y} \\ \dot{z} \end{bmatrix}. \tag{36}$$

Due to the constrain of revolution joints, the motions in x, y, and θ_z are constrained. Thus, the stiffness matrix can be

https://doi.org/10.1017/S0263574711000683 Published online by Cambridge University Press

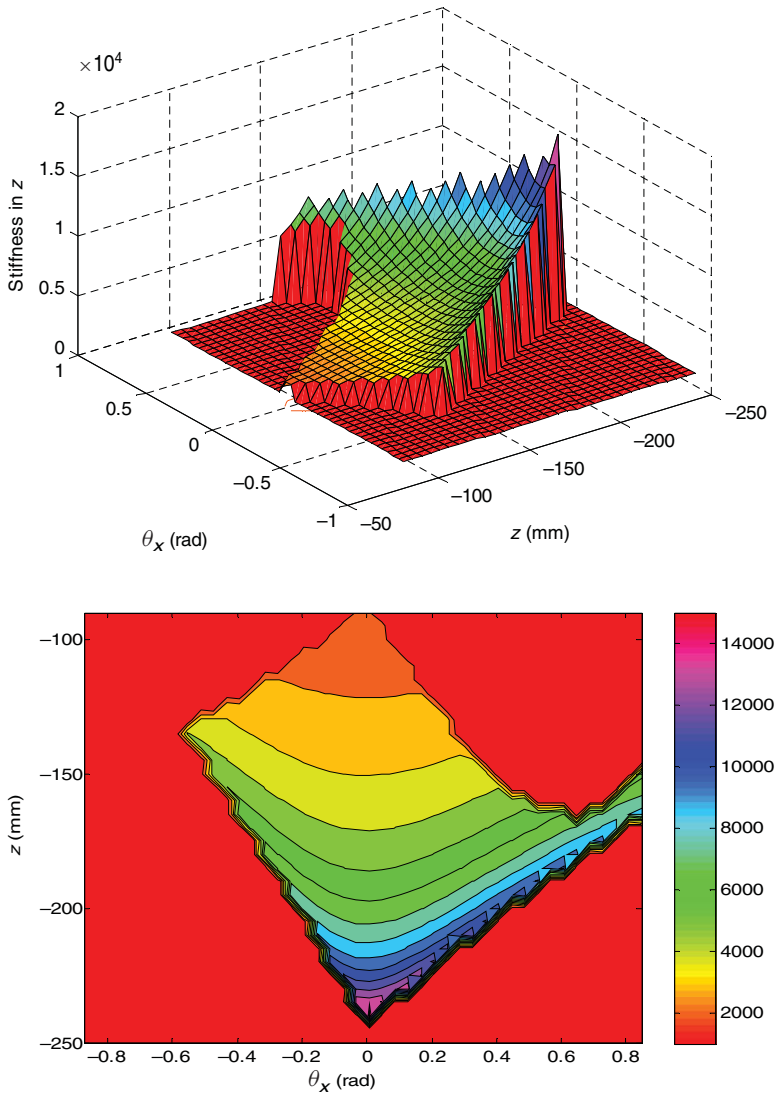

Fig. 14. (Colour online) z stiffness distribution along θ_x and z (when $\theta_y = 0$).

Table I. Architecture parameters.

l_p	204 mm
l_n	178 mm
l_{1i}	245 mm
d	250 mm
α_i	$(-30^\circ, 90^\circ, 120^\circ)$
β_i	$(-30^\circ, 90^\circ, 120^\circ)$

simplified into a 3×3 matrix

$$\begin{bmatrix} \tau_x \\ \tau_y \\ F_z \end{bmatrix} = \begin{bmatrix} k_{11} & k_{12} & k_{13} \\ k_{21} & k_{22} & k_{23} \\ k_{31} & k_{32} & k_{33} \end{bmatrix} \begin{bmatrix} \dot{\theta}_x \\ \dot{\theta}_y \\ \dot{z} \end{bmatrix}. \tag{37}$$

The stiffness matrix can be generated from Eq. (35), in which the Jacobian matrix and inverse kinematics can be obtained from Sections 3.3 and 3.4. The units of terms in stiffness matrix are N/mm for k_{33}, N mm/rad for k_{11}, k_{12}, k_{21}, and k_{22}, N mm/mm for k_{13} and k_{23}, and N/rad for k_{31} and k_{32}. Here, k_{11}, k_{22}, and k_{33} are pure stiffness, which represent the torques or forces are affected by the deformation at the same directions, which are the dominant terms in the stiffness matrix, while other terms are less important, so they can be neglected.

The distribution of k_{11}—the stiffness in θ_x caused by the deformation of θ_x—along θ_x and θ_y is shown in Fig. 7. Numerical simulation results show that θ_x stiffness decreases with the increase of θ_x. The stiffness is symmetry distributed along $\theta_y = 0$, the stiffness has minimum values when $\theta_y = 0$. Figures 8 and 9 reveal θ_x stiffness distribution along θ_x, z directions and θ_y, z directions, which show the PKM has higher θ_x stiffness as z increases.

Figures 10–12 represent the distributions of θ_y stiffness k_{22} along θ_x, θ_y, and z directions. Similar as θ_x stiffness, the θ_y stiffness increases with the growth of θ_x, until arrives the maximum point at bounds. While it reaches the bottom at $\theta_y = 0$. As for the distributions along z-axis, the θ_y stiffness increases when z has higher values.

https://doi.org/10.1017/S0263574711000683 Published online by Cambridge University Press

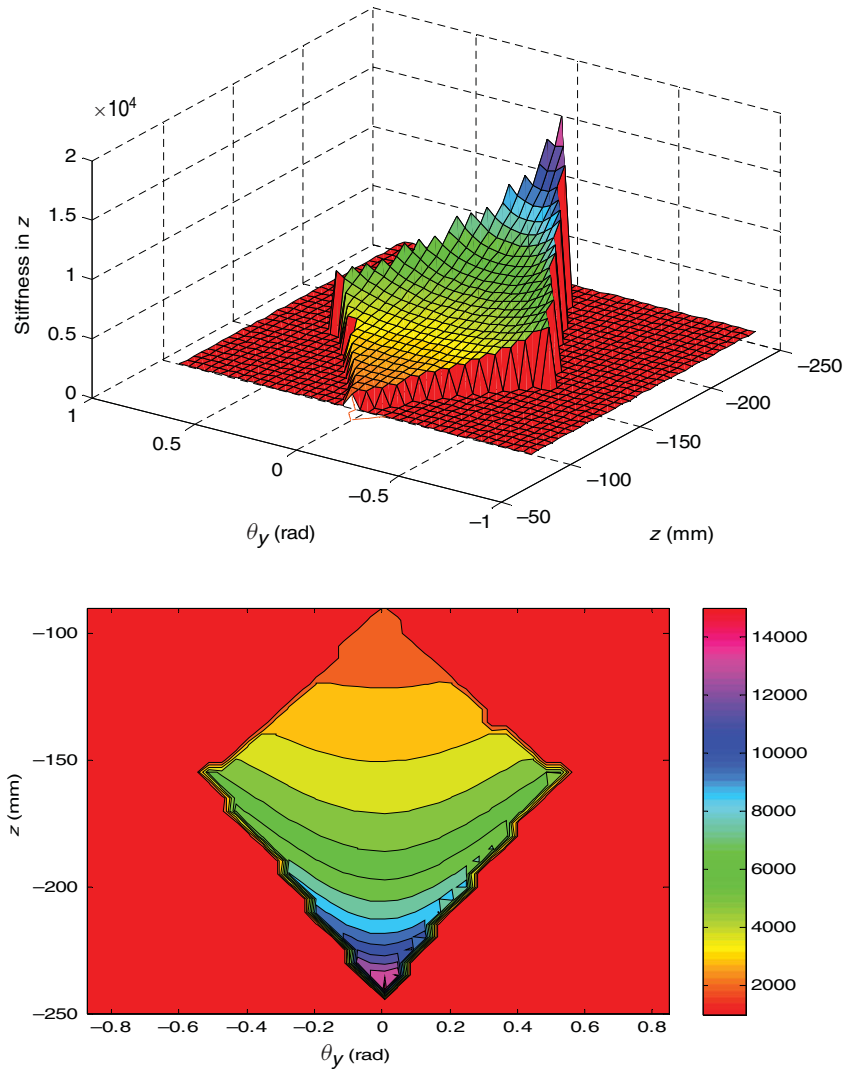

Fig. 15. (Colour online) z stiffness distribution along θ_y and z (when $\theta_x = 0$).

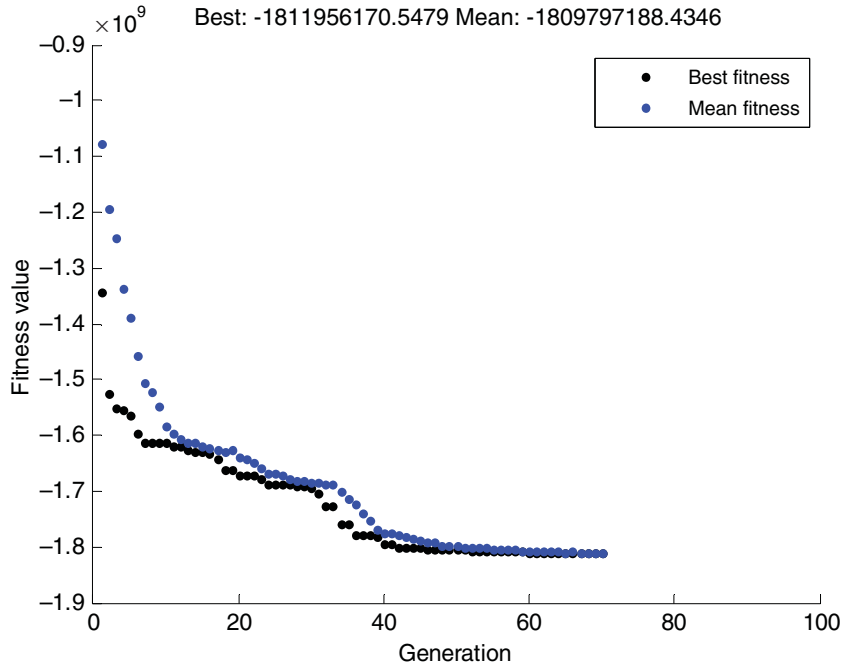

Fig. 16. (Colour online) Optimization result of k using GA.

https://doi.org/10.1017/S0263574711000683 Published online by Cambridge University Press

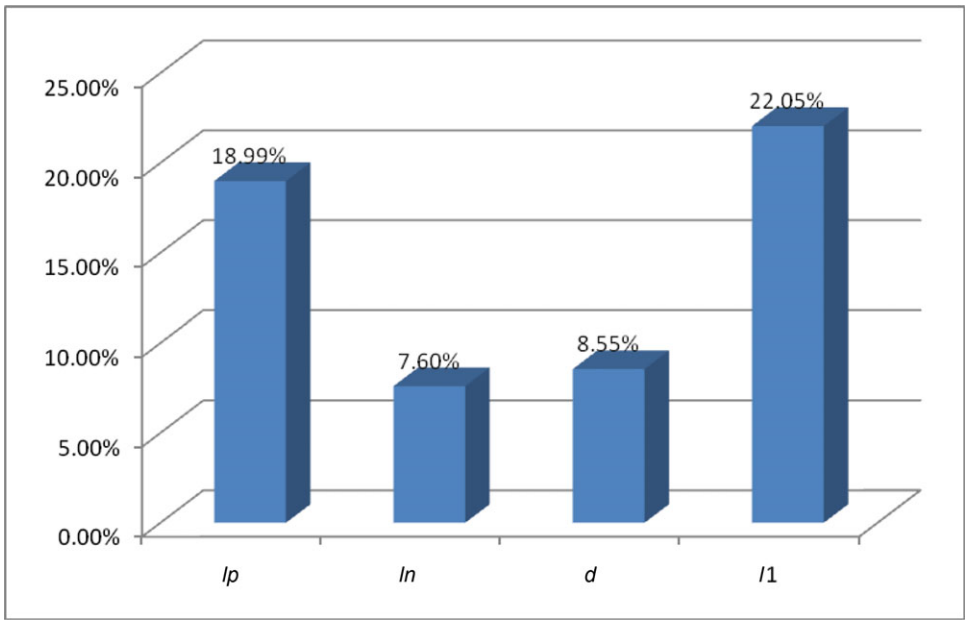

Fig. 17. (Colour online) Effect of design variables on increasing the stiffness of PKM.

From Figs. 13–15, the z stiffness gets minimum point when $\theta_x = \theta_y = 0$, while along z, it grows as z increases.

5. Optimization

By the analysis above, the stiffness distribution is revealed in the domain with two variables, when the third one is supposed to be fixed. If the three variables are to be considered simultaneously, it is very hard to predict the trends of the stiffness changes. Therefore, the optimization method should be used to find the optimal parameters of the PKM including the sizes of the base and end-effector, length of the legs, and the angle of the actuators based on stiffness control.

The Genetic Algorithms (GAs) are selected as optimization method. The GAs are global search methods that are based on the Darwin's principle of natural selection and genetic modification, which operates with a population of possible solutions (individuals) of the optimization problem. These solutions are evaluated with respect to their degree of fitness that indicates how well the individuals will fit the optimization problem. In the stiffness matrix, the dominant elements are k_{11}, k_{22}, and k_{33}, which can be considered as the main stiffness effects in θ_x, θ_y, and z. Here, they are denoted by $k_{\theta x}$, $k_{\theta y}$, and k_z. Thus, the design optimization problem can be described as

Maximize:

$$k = \text{trace}(k) = k_{11} + k_{22} + k_{33} = f(l_p, l_n, d, l_1), \quad (38)$$

Subject to:

$$\begin{cases} 204 \text{ mm} \le l_p \le 224 \text{ mm}, \\ 130 \text{ mm} \le l_n \le 143 \text{ mm}, \\ 130 \text{ mm} \le d \le 160 \text{ mm}, \\ 245 \text{ mm} \le l \le 270 \text{ mm}. \end{cases} \quad (39)$$

Table II. Optimal design variables based on GA for maximizing k.

Optimal values	1st	2nd	3rd
k	1.8115e9	1.8117e9	1.8089e9
l_p (mm)	223.996	223.997	224.000
l_n (mm)	130.014	130.002	130.010
d (mm)	158.453	159.082	157.892
l_1 (mm)	245.000	245.002	245.019

The MATLAB GA toolbox is selected to implement this design optimization. After 64 generations, the objective function(38) is convergent to maximum point as shown in Fig. 16 and the best variables are revealed in Table II.

As shown in Fig. 17, increasing end-effector size l_p from 214 to 224 mm leads to a growth of stiffness by 18.99%, while optimizing the base platform size l_n from 136.5 to 130 mm and the distance between base platform and middle moving platform from 145 to 151 mm raises the stiffness by 7.6 and 8.55%, respectively. The most effective way is to reduce the length of the active links, which leads to an increase of the stiffness by 22.05%.

6. Conclusion

This paper develops a new reconfigurable tripod parallel manipulator design that aims to increase the accuracy and stiffness of the machine. The stiffness model is derived based on the inverse kinematic analysis and Jacobian matrix considering all the links are rigid bodies and the parasitic motions can be neglected. Also, the stiffness distributions in three different directions θ_x, θ_y, and z are performed in two-dimensional workspaces. On the basis of the stiffness analysis, the stiffness optimization is generated. By revising the machine parameters, the stiffness of this reconfigurable PKM is greatly improved.

https://doi.org/10.1017/S0263574711000683 Published online by Cambridge University Press

Acknowledgments

The authors would like to acknowledge the financial support from the Natural Sciences and Engineering Research Council of Canada (NSERC). The second author gratefully acknowledges the financial support from Canada Research Chairs program.

References

1. J. P. Merlet, *Parallel Robots* (KIuwer Academic Publishers, Dordrecht, Netherlands, 2000).
2. D. Zhang, Z. Bi and B. Li, "Design and kinetostatic analysis of a new parallel manipulator," *Int. J. Robot. Comput.-Integr. Manuf.* **25**, 782–791 (2009).
3. Z. Chi and D. Zhang, "Motion Plan of a Parallel Kinematic Machine Based on Stiffness Control, 2010," *Proceedings of the International Design Engineering Technical Conferences and Computers and Information in Engineering Conference*, Montreal, Quebec, Canada (Aug. 15–18, 2010) pp. 1219–1258.
4. T. Huang, J. P. Mei, X. Y. Zhao, L. H. Zhou, D. W. Zhang and Z. P. Zeng, "Stiffness Estimation of a Tripod-Based Parallel Kinematic Machine," *Proceedings of the IEEE International Conference on Robotics and Automation*, Seoul Korea (2001) pp. 3280–3285.
5. L. W. Tsai, "The stewart platform of general geometry has 40 configurations," *J. Mech. Des.* **115**(2), 277–283 (Jun. 1993).
6. E. F. Fichter, "A stewart platform- based manipulator: General theory and practical construction," *Int. J. Robot. Res.* **5**, 157–182 (1986).
7. F. Pierrot, C. Reynaud and A. Fournier, "DELTA: A simple and efficient parallel robot," *Robotica* **8**, 105–109 (1990).
8. L. W. Tsai, "Kinematics and optimization of a spatial 3-UPU parallel manipulator," *J. Mech. Des.* **122**(4), 439–448 (Dec. 2000).
9. Y. Li and Q. Xu, "Design and analysis of a new singularity-free three-prismatic-revolute-cylindrical translational parallel manipulator," *J. Mech. Eng. Sci.* **221**, 565–577 (Dec. 2005).
10. Y. Li and Q. Xu, "A novel design of a 3-PRC translational compliant parallel micromanipulator for nanomanipulation," *Robotica* **24**, 527–528 (2006).
11. Y. Li and Q. Xu, "Kinematic analysis and design of a new 3-DOF translational parallel manipulator," *J. Mech. Des.* **128**, 729–737 (2006).
12. Y. Li and Q. Xu, "Kinematic analysis of a 3-PRS parallel manipulator," *Robot. Comput.-Integr. Manuf.* **23**, 395–408 (2007).
13. X. Kong and C. M. Gosselin, "Kinematics and singularity analysis of a novel type of 3-CRR 3-DOF translational parallel manipulator," *Int. J. Robot. Res.* **21**, 791–799 (2002).
14. Y. Koren, U. Heisel, F. Joveane, T. Morwaki, G. Pritschow, G. Ulsoy and H. Van Brussel, "Reconfigurable manufacturing systems," *Ann. CIRP* **48**(2), 527–541.
15. M. Li, T. Huang, J. Mei and X. Zhao, "Dynamic formulation and performance comparison of the 3-DOF modules of two reconfigurable PKM-the tricept and the trivariant," *Trans. ASME J. Mech. Des.* **127**(5), 1129–1136 (2005).
16. T. Huang, M. Li, M. Zhao, J. P. Mei, Chetwynd and S. J. Hu, "Conceptual design and dimensional synthesis for a 3-DOF module of the TriVariant-A novel 5-DOF reconfigurable hybrid robot," *IEEE Transations Robot.* **21**(3), 449–456 (Jun. 2005).
17. Z. M. Bi, S. Y. T. Lang, M. Verner and P. Orban, "Development of reconfigurable machines," *Int. J. Manuf. Technol.* **39**, 1227–1251 (2008).
18. Z. M. Bi, W. A. Gruver, W. J. Zhang and S. Y. T. Lang, "Automated modeling of modular robotic configurations," *Int. J. Robot. Auton. Syst.* **54**, 1015–1025 (2006).
19. T. Huang, J. P. Mei and X. Y. Zhao, "Stiffness Estimation of a Tripod-based Parallel Kinematic Machine," *Proceedings of the International Conference on Robotics and Automation*, Seoul, Korea (May 21–26, 2001) pp. 50–58.
20. C. Gosselin, "Stiffness mapping for parallel manipulators," *IEEE Trans. Robot. Autom.* **6**(3), 377–382 (Jun 1990).
21. B. S. EI-Khasawneh and P. M. Ferreira, "Computation of stiffness bounds for parallel link manipulators," *Int. J. Mach. Tools Manuf.* **39**, 321–342 (1999).
22. Y. Li and Q. Xu, "Stiffness analysis for a 3-PUU parallel kinematic machine," *Mech. Mach. Theory* **43**, 186–200 (2008).